Available online at www.sciencedirect.com
SCIENCE DIRECT
Superlattices and Microstructures 39 (2006) 501–516
Superlattices and Microstructures
www.elsevier.com/locate/superlattices

Raman scattering from acoustic modes in Si/Ge superlattice waveguides

Ricardo Claps[a,*], Dimitrios Dimitropoulos[a], Bahram Jalali[a], Bernard Jusserand[b]

[a] *Optoelectronic Circuit and Systems Laboratory, ENG IV UCLA, 420 Westwood Plaza, Los Angeles, CA 90095, USA*
[b] *Institut des Nanosciences de Paris, Université Pierre et Marie Curie, UMR CNRS 7588, Campus Boucicaut, 140 Rue de Lourmel, 75015 Paris, France*

Received 17 September 2005; received in revised form 12 November 2005; accepted 6 January 2006
Available online 3 March 2006

Abstract

This paper discusses the design of acoustic vibrational modes in Si/Ge planar optical waveguides and its application in creating silicon-based Raman devices with a flexible spectrum. It addresses the deficiencies of the recently demonstrated Raman-based silicon lasers and amplifiers as they relate to spectral and low efficiency limitations of bulk silicon. The treatment is for in-plane scattering in a forward scattering configuration. In addition to calculating the spectrum and the efficiency for Raman active modes, it is shown that the negligible wave-vector of the phonons involved in this type of scattering allows for the use of the bandgap "pinching" effect to arrive at specific layer thicknesses for Si and Ge that optimize the scattering efficiency.

Keywords: Silicon germanium superlattices; Acoustic phonons; Photoelastic effect in superlattices; Phonon engineering; Brillouin scattering

1. Motivation

The use of Raman nonlinear processes in silicon waveguides has emerged as a promising means to create optically active devices in silicon including amplifiers, lasers and

* Corresponding address: Neptec Optical Solutions, 48603 Warm Springs Blvd. Fremont, CA 94539, United States. Tel.: +1 865 591 4682; fax: +1 510 687 0599.
E-mail address: claps@ee.ucla.edu (R. Claps).

0749-6036/$ - see front matter © 2006 Elsevier Ltd. All rights reserved.
doi:10.1016/j.spmi.2006.01.001

wavelength converters [1–5]. Several areas of improvement remain, namely: waveguide side-wall smoothening [6], reduced waveguide dimensions [7], and low-loss fiber-to-waveguide coupling [8]. Other approaches to take advantage of the Raman effect have been suggested, such as the use of micro-ring resonators [9,10], and complex resonant structures [11]. However, the use of Raman nonlinearities in silicon is ultimately limited by the vibrational spectrum of the bulk material. There are three fundamental parameters that cannot be changed by fabrication or design, if one is bound to the use of bulk silicon as the active medium. These are: Raman scattering strength, resonant bandwidth, and spectral range. The main goal of this paper is to demonstrate that the silicon–germanium platform (SGP) is a powerful tool for modifying these aspects of the Raman effect, which directly relate to the performance and capabilities of silicon-based devices that take advantage of Stimulated Brillouin/Raman Scattering (SBRS) and Coherent anti-Stokes Raman Scattering (CARS). The SGP is compatible with baseline silicon chip manufacturing and is being considered for next generation CMOS integrated circuits. The underlying reason for the use of SGP in CMOS is the high electron–hole mobility in germanium, compared to that of silicon. Recent development of stressed-silicon layers built on top of silicon–germanium substrates, have demonstrated the fastest MOSFET devices to date [12], boosting the prospects for SGP in the next generation integrated-circuits. Added to its useful physical properties, the introduction of germanium in silicon foundries is a “non-disruptive” process that does not pose contamination issues.

The use of phonon engineering in silicon/germanium superlattices (SGSL’s) has been suggested by Soref et al., in the context of tera-Hertz wave generation, using a quantum cascade laser structure [13]. In addition, the Raman spectra of SGSL’s have also been studied [14–18]. In these studies, Raman scattering was used as a diagnostic tool to extract information about the composition, geometry and quality of the hetero-structures, which were intended to produce materials with a direct electronic bandgap [19,20]. Most studies were performed on back-scattering configurations along the perpendicular direction relative to the plane of the SGSL layer growth. Abstreiter et al. [21], and others [22], have performed a thorough study of different Raman back-scattering configurations in such systems.

In the present paper, we consider the problem of engineering the Raman spectrum and efficiency of silicon-based Raman devices by using SGSL structures to realize Raman-active acoustic vibrational modes. The focus is on Raman scattering in planar waveguides with a SGSL core; the type of structures that would be used in a waveguide Raman amplifier or laser. The paper presents the treatment for in-plane scattering in a forward scattering configuration. In addition to calculating the spectrum and the efficiency of Raman-active modes, it is suggested that the negligible wave-vector of phonons involved in this type of scattering allows for the use of the bandgap “pinching” effect [23,24] to arrive at specific layer thicknesses for Si and Ge that optimize the scattering efficiency.

2. Theory and model

The geometry of interest in the case considered in this work will be linear scattering, forward and backward, along the direction of the plane of the superlattice, which will be assumed to grow along the (001) direction of the crystal. This configuration lends itself more easily for waveguide fabrication, in terms of layer growth, lithography and material deposition, and also from the optical confinement point of view.

This paper will not deal with the issues of optical mode-confinement and propagation in a SGSL-based waveguide, but only with the spectral properties of light scattering in the given

configuration. Therefore, the study of the optical properties of such waveguides is outside the scope of the present work. Furthermore, the SGSL will be considered to be defect-free and to extend to infinity along the growth direction. From here on, all optical fields will be assumed to be plane waves traveling along the in-plane superlattice direction, through an infinite SGSL. The analysis has to begin from the study of the dispersion properties of phonon waves in these structures. The first issue that needs to be considered is the zone-folding effect, which appears as a result of the long range periodicity imposed in the crystal by the superlattice structure [25].

The theoretical treatment of folded phonon modes (FPM) has to be divided between folded optical-phonon modes (FOPM) and folded acoustic-phonon modes (FAPM). The reason for this is the fact that the Raman scattering process for FOPMs takes place at a microscopic level, within the unit cell of the superlattice crystal. The overall resulting process is just the summation of the scattered radiation from all the individual unit cells in the crystal. Therefore, a molecular bond-polarizability model for the scattering process is appropriate in this case [26,27]. In this model, a suitable Raman tensor, which contains the reduced symmetry of the SGSL, determines the coupling between the optical fields and the vibrations of the material.

In the case of FAPMs, the Raman scattering resulting from these modes has its origin in the photoelastic interaction [28]. This interaction arises from the long-range strain induced in the material by the confined FAPMs, and therefore it is not spatially constrained to the unit cell of the superlattice. The coupling of the optical fields to the vibration of the atoms is governed by the photoelastic tensor, in the same manner as bulk Brillouin scattering is. However, an important difference between bulk Brillouin scattering and superlattice Brillouin scattering needs to be mentioned. In the case of a superlattice, forward Brillouin scattering is allowed, because the confinement of the FAPMs provides phonon states with finite frequency at zone-center. The present paper will focus on the theoretical analysis of the Raman spectrum from FAPMs in SGSL's along the in-plane propagation direction. Section 2.1 will discuss the dynamics of FAPMs, namely their dispersion properties, and Section 2.2 will treat the coupling of the optical fields and the FAPMs. The treatment of FOPMs using the bond-polarizability theory will be left out of the present analysis, since the approach and methodology is quite different in this case. Finally, Section 2.3 will be devoted to the perspectives for the use of the results in Section 2.2 to design optical amplifiers, lasers, and wavelength converters based on the Brillouin/Raman effect.

2.1. Continuum model for folded acoustic-phonon modes

We start from constructing the FAPMs of a SGSL along the in-plane direction, using a well-known continuum model for the propagation of vibrations in a solid [28]. This model was first proposed and derived by Rytov [29], and used in the calculation of dispersion relations for sagittal waves in superlattices by Djafari-Rouhani et al., in the context of acoustic surface-mode propagation [30]. The model assumes a continuous wave function, $\vec{\Psi}(\vec{x})$, to represent the displacement field of a traveling wave in the material, at point $\vec{x}$. The physical meaning of this function is that atoms in the vicinity of point $\vec{x}$ in the crystal are displaced, on average, by a vector, $\vec{\Psi}$, about their "equilibrium" (zero force) positions. Fig. 1 shows the geometry of the problem, with the SGSL grown along the z-axis, assuming a Si layer of thickness, d_a, and a Ge layer of thickness, d_b ($d_b = d - d_a$). For the remainder of this paper, all parameters relative to silicon will be labeled with subscript "a" and those corresponding to germanium, with subscript "b". The periodicity of the SGSL along the z-direction allows us to impose Bloch's condition on the field component, Ψ_j, as

$$\psi_j^{k_z}(x, y, z + d) = \mathrm{e}^{\mathrm{i}k_z d}\psi_j^{k_z}(x, y, z); \quad 0 \le z \le d = d_a + d_b \tag{1}$$

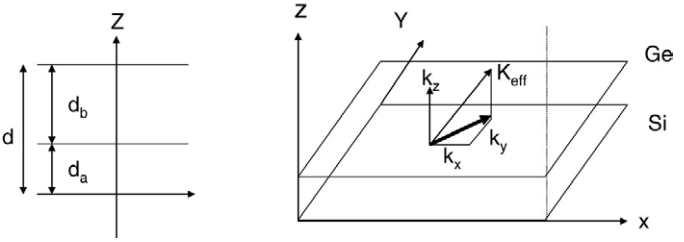

Fig. 1. Geometry selected for the analysis of the SGSL. A germanium layer of thickness, d_b, is grown on top of a silicon layer of thickness, d_a. Plane waves propagating in the xy plane acquire a momentum component, k_z, along the z-direction, as expressed in Bloch's theorem.

Table 1
Elastic constants of Si and Ge[a] ($\times 10^{12}$ dyne/cm^2)

	Si	Ge
C_{11}	1.66	1.285
C_{12}	0.639	0.483
C_{44}	0.796	0.680

[a] P.Y.Y. Yu, M. Cardona; "Fundamentals of Semiconductors", Ch. 3 p. 141. Taken from: O. Madelung, M. Schulz, H. Weiss: Landolt-Bornstein, Series III, Vol. 22, Subvolume a. Intrinsic Properties of Group IV Elements, III–V, II–VI, and I–VII Compounds (Springer, Berlin, Heidelberg, 1987).

where d is the SGSL period, shown in Fig. 1, and k_z is the Bloch wave-vector. The dynamical behavior of the field, $\vec{\Psi}(\vec{x})$, is expressed by the Christoffel equation, which is written as follows [25]

$$\rho\omega^2\vec{\psi} = \nabla\cdot\bar{\chi} = \nabla\cdot(\bar{C}\otimes\bar{e}). \tag{2}$$

where ρ, is the density of the material and ω, the associated frequency of oscillation of a given mode, $\vec{\Psi}(\omega)$. In Eq. (2), $\bar{\chi}$, is the stress tensor for the crystal, which is given in terms of the stiffness tensor, $\bar{C}$, and the strain tensor, $\bar{e} = \frac{1}{2}(\nabla\vec{\psi} + \nabla^t\vec{\psi})$. For a crystal with cubic-symmetry, as is the case for the individual Si and Ge layers considered here, the tensor, $\bar{C}$, has only 3 independent components, c_{11}, c_{12}, and c_{44} [25]. The values used for the constants, c_{ij}, in the ensuing calculations are listed in Table 1, below. The field solutions, $\vec{\psi}(\vec{x})$, for any given value of $\vec{k} = (k_x, k_y, k_z)$, are construed in the usual manner, as plane waves traveling in opposite directions,

$$\Psi_j(x,y,z) = \begin{cases} \psi_j^{+a}\mathrm{e}^{\mathrm{i}(k_x x+k_y y)+\mathrm{i}\frac{\omega}{va}z} + \psi_j^{-a}\mathrm{e}^{-\mathrm{i}(k_x x+k_y y)-\mathrm{i}\frac{\omega}{va}z}, & 0 < z < d_a. \\ \psi_j^{+b}\mathrm{e}^{\mathrm{i}(k_x x+k_y y)+\mathrm{i}\frac{\omega}{vb}z} + \psi_j^{-b}\mathrm{e}^{-\mathrm{i}(k_x x+k_y y)-\mathrm{i}\frac{\omega}{vb}z}, & d_a < z < d. \end{cases} \tag{3}$$

For $j = 1, 2, 3$ the coefficients $\psi_j^{\pm a}$ are to be determined by the Bloch conditions imposed from Eq. (1) and the continuity of the fields at the boundary between Si and Ge, $z = d_a$, and $z = 0$. Furthermore, the derivatives of the fields also have to obey similar conditions, since they are related to the stress tensor, $\bar{\chi} = \bar{C}\otimes\bar{e}$, which is a physical property of the material. The conditions to be satisfied are thus, for any value of $\vec{k}$ [25,31],

$$\begin{aligned} &\psi_j^a(\vec{k}, d_a) = \psi_j^b(\vec{k}, 0), \quad \mathrm{e}^{\mathrm{i}k_z d}\psi_j^a(\vec{k}, 0) = \psi_j^b(\vec{k}, d_b), \\ &\bar{\chi}_{ij}^a(\vec{k}, d_a) = \bar{\chi}_{ij}^b(\vec{k}, 0), \quad \mathrm{e}^{\mathrm{i}k_z d}\bar{\chi}_{ij}^a(\vec{k}, 0) = \bar{\chi}_{ij}^b(\vec{k}, d_b). \end{aligned} \tag{4}$$

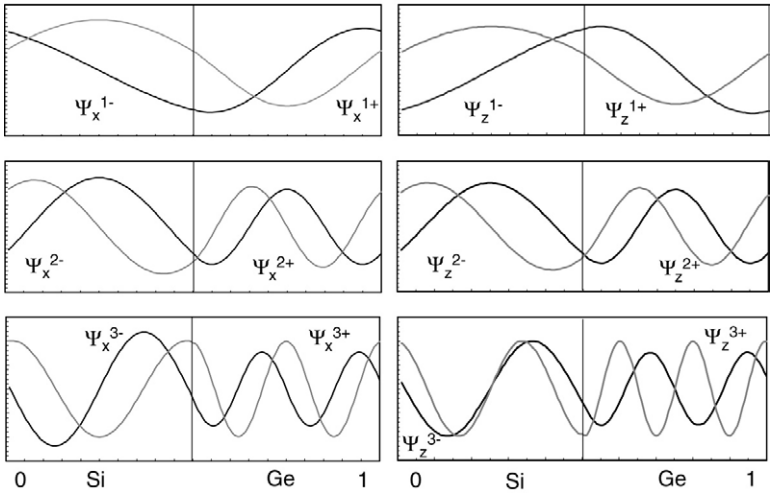

Fig. 2. Acoustic mode displacements along the z- and x-axes. The direction of propagation of the waves is the x-axis; in this particular case it is assumed that, without loss of generality, $\vec{k} = 0\,(k_x = 0, k_z = 0.01(1/d))$. The horizontal scale denotes the position along the z-axis, and the vertical scale is the normalized amplitude of the displacement. The SGSL has $d_a = d_b = 0.5$. All wave-functions are normalized. See text for details on notation.

Expression (4) leads to a set of 12 linear, homogeneous equations. The solutions for the wave-vectors and wave-functions are obtained by finding the kernel of the 12×12 matrix resulting from this system. For the in-plane propagation problem, the system can be separated into a transverse solution (4×4 matrix), and a longitudinal–transverse solution (8×8 matrix). Fig. 2 shows some of the solutions to Eqs. (2) and (4), denoted as $\Psi_i^{\pm N}(0, 0, z)$, with propagation vector, $\vec{k} = k_x\hat{x}$, along the x-axis, and $i = x, z$. The superscript $\pm$ and the label, $N = 1$, 2 and 3, refer to the dispersion properties of the waves at zone-center, as will be explained below.

From the wave-functions shown in Fig. 2 a number of important thermo-acoustic properties of the SGSL, along the in-plane direction, can be derived, e.g. the stress properties and the phonon-transfer matrix, which is used to calculate the properties of "phononic crystals", as described in detail by Mizuno and Tamura [32]. The oscillation frequency, ω, of the acoustic waves is ultimately determined by the stiffness coefficients (Table 1), the density, ρ, of the materials involved, and the periodicity, d, of the SGSL being used. The relation, for in-plane propagating acoustic waves, can be derived from Eq. (2) as:

$$\nu_L = \frac{\omega}{2\pi} = \sqrt{C_{11}/\rho} \cdot (1/d), \tag{5a}$$

$$\nu_T = \frac{\omega}{2\pi} = \sqrt{C_{44}/\rho} \cdot (1/d), \tag{5b}$$

where ν_L and ν_T denote longitudinal and transverse waves, respectively. Eqs. (5a) and (5b) are valid for propagation along the X- or Y-axes ([100] and [010] directions in the crystal). For the rest of this work, a periodicity of $d = 100$ nm will be assumed for the SGSL. This comprises several tens of monolayers of both Si and Ge. The underlying assumption is that, to within ~10 monolayers, the structure behaves mechanically and optically as the bulk of the material; this will be called the Macroscopic Hypothesis. Although a challenging task, fabrication of SGSL structures with a thickness of a few 100's nm falls within state-of-the-art capabilities. Also, optical waveguides well in the sub-micron regime are feasible, with propagation losses below

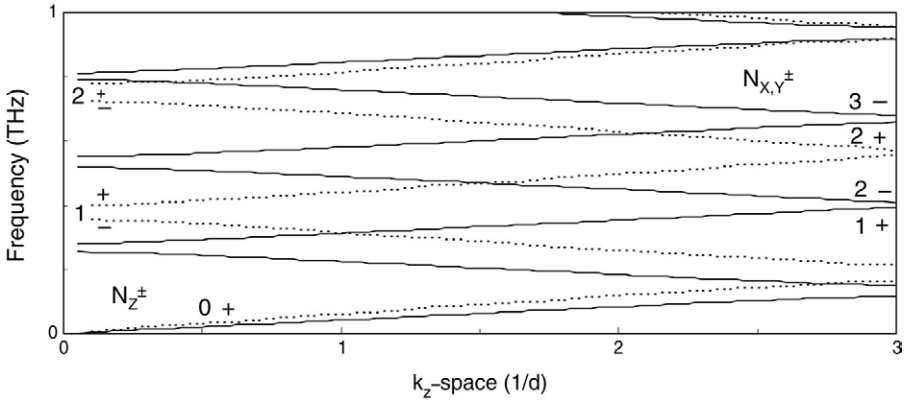

Fig. 3. Dispersion of longitudinal-FAPM ($\Psi_z^{\pm N}$-dashed lines-) and transverse-FAPM ($\Psi_x^{\pm N}$, $\Psi_y^{\pm N}$-continuous lines-). The k_z component is the Bloch wave-vector. The index $N_{Z(XY)}$ relates to the longitudinal (transverse) modes.

0.5 dB/cm [33]. Having selected the dimension of the SGSL, a frequency scale can be established for the rest of the analysis. Note that the physical content of the results that will be presented is independent of the specific periodicity of the SGSL, but relies essentially on the validity of the Macroscopic Hypothesis.

Fig. 3 shows the dispersion of the longitudinal and transversal-FAPMs, $\Psi_z^{\pm N}$ and $\Psi_{x,y}^{\pm N}$, respectively, with propagation vector along the growth direction, $\vec{k} = k_z\hat{z}$. This is the classical behavior observed for periodic systems, where the appearance of bandgaps at zone-center is manifest. These bandgaps have been labeled (N), according to their order of appearance relative to zero frequency. Also, the bands branching from the gaps have been labeled "+", on the higher frequency end of the gap, and "−" on the lower frequency end. The Brillouin zone edge, in the z-direction, is $k_z = \pi/d$. The wave-functions follow the same labeling notation, adding the suffix X, Y or Z, regarding the axis of *displacement* of the mode, at *zone-center*. Fig. 4 shows the dispersion relation obtained for FAPMs with propagation wave-vector, $\vec{k} = k_x\hat{x}$. In this case, however, the Brillouin zone is much larger, since the edge occurs at $k_x = \pi/a$, where a, is the lattice constant of the bulk crystal (Si/Ge). The waves shown have a displacement field in the x–z plane, $\vec{\Psi}^{\pm N} = (\Psi_x^{\pm N}, 0, \Psi_z^{\pm N})$; as will be shown in Section 2.2, these are the relevant components for the in-plane optical activity of a SGSL waveguide. These waves are orthogonal at zone-center, but as the magnitude of the k_x vector increases, there is mixing between the two sets of wave-functions ($\Psi_x^{\pm N}$, and $\Psi_z^{\pm N}$), as will be discussed in Section 2.3. At zone-center, the gap for each set of wave-functions, $\Psi_x^{\pm N}$, and $\Psi_z^{\pm N}$, with $\vec{k}$ along the X-direction, coincides with the gap from the dispersion of the corresponding wave, with $\vec{k}$ along the Z-direction (Fig. 5), in terms of the displacement of the wave relative to $\vec{k}$ (longitudinal–transversal). The in-plane phonon-dispersion relations are also useful for calculating heat-transfer properties of SL systems. Combining the results shown in Fig. 4 with the phonon density of states, which can be derived from a general solution of Eq. (4), the Boltzmann transfer equation (BTE) can be used to investigate the use of SGSL's in thermo-electric devices, following previous work on similar structures [34–37]. Fig. 5 shows a detail of the dispersion curves of the four acoustic-phonon wave-functions in the 0.5–1.0 THz frequency range. The states chosen correspond to $N_z = 2$, $N_{x,y} = 3$, at 0.8 THz, from Figs. 3 and 4. The frequency gaps at zone-center clearly match the longitudinal and transversal mode dispersions along the z-direction.

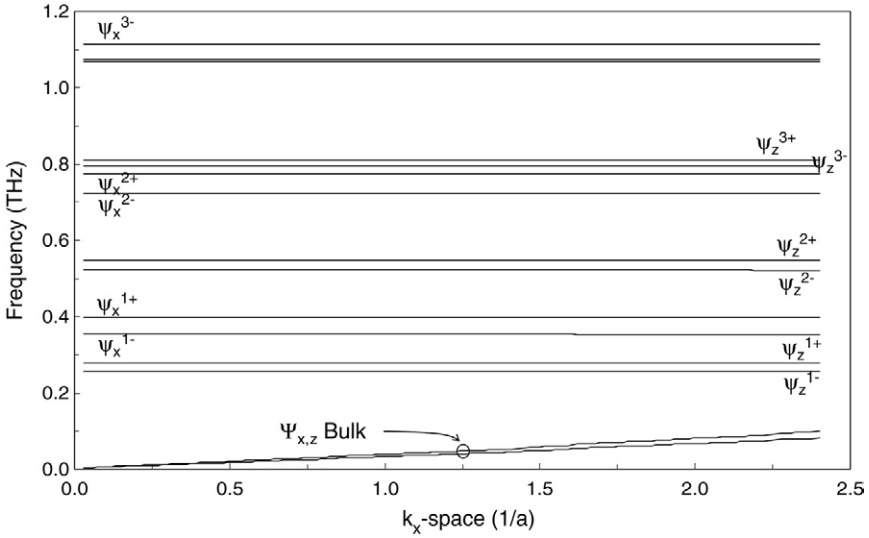

Fig. 4. Dispersion relation for FAPMs propagating along the x-axis for a SGSL with $d_a = d_b$. Only phonons with displacement vector in the x–z plane are illustrated.

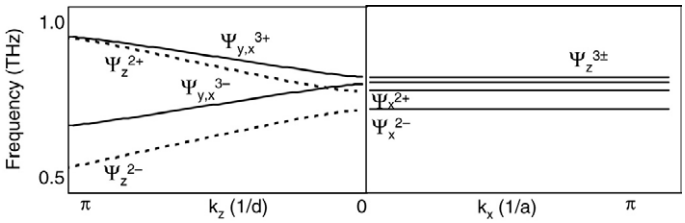

Fig. 5. Detail of the modes in the 0.5 to 1.0 THz range, from Fig. 4. The four (x–z) modes are clearly seen for $\vec{k}$ along the x-direction. The dispersion of acoustic modes along the k_z-direction is overlaid to illustrate the discussion in the text.

2.2. Photoelastic scattering from folded acoustic-phonon modes

The photoelastic interaction arises by the strain-induced dipole moment produced by long-range vibrations in a crystal, in the presence of an electric field. These vibrations are low-frequency, acoustic modes, which in bulk materials behave like sound waves traveling through the crystal. As we have seen in Section 2.1, the dynamics of FAPMs is quite different, but the essence of the photoelastic process remains the same, since the material displacements are unchanged at the microscopic level. It is important to stress at this point that this is a hypothesis, and much of the details are still unclear. Furthermore, much research has been devoted to design hetero-structures in such a way as to precisely change the nature of the FAPMs at the microscopic level [38–40]. However, experimental results so far seem to qualitatively confirm the photoelastic model, which is governed by the fourth-rank, photoelastic tensor, $\bar{\pi}$, defined as

$$p_j = \bar{\pi}_{jlmi} \otimes \bar{e}_{lm} \cdot E_i. \tag{6}$$

Eq. (6) means that the induced polarization, $\vec{p}$, is the result of the interaction of the incident electric field, $\vec{E}$, with the strain, $\bar{e}_{lm}$, induced in the crystal by the oscillation of the acoustic

Table 2
Photoelastic constants of Si and Ge

	Si[a] (3.4 μm)	Ge[b] (3.4 μm)
π_{11}	−0.153	−0.151
π_{12}	0.017	−0.128
π_{44}	−0.051	−0.072

[a] M.J. Weber, CRC Handbook of Laser Science and Technology.
[b] A. Feldman, R.M. Waxler, D. Horwitz, "Photoelastic constants of germanium", J. Appl. Phys. 49 (4) 2589–2590 (1978).

modes ψ_l and ψ_m (see definition of $\bar{e}_{lm}$ in Section 2.1 above). In the reduced notation, for a crystal with cubic symmetry, the only non-zero components of $\bar{\pi}$ are: π_{11}, π_{12}, and π_{44} [41]. Using this notation, Eq. (6) can be conveniently written in terms of component vectors as

$$p_j \propto \frac{1}{2}\pi_{44}\{(\bar{k}\cdot\hat{e})\psi_j + (\vec{\psi}\cdot\hat{e})k_j\} + \pi_{12}(\vec{k}\cdot\vec{\psi})e_j + (\pi_{11}-\pi_{12}-\pi_{44})b_j \tag{7}$$

where $\hat{e}_i$ is the unit vector in the direction of the optical field polarization, $\vec{k}$, is the phonon momentum vector, and $\vec{b}$ is defined by,

$$\vec{b} = (\psi_x k_x \hat{e}_x, \psi_y k_y \hat{e}_y, \psi_z k_z \hat{e}_z).$$

The values of the photoelastic coefficients, π_{ij}, for silicon and germanium are shown in Table 2 below, all measured at a wavelength, $\lambda = 3.4$ μm. This wavelength is well below the bandgap for silicon and also germanium, so dispersion effects are not expected in the region of interest for this work ($\lambda = 1.5$ μm), at least for silicon. However, at this wavelength range, germanium absorption starts to manifest strongly, so an accurate value of π_{ij} for germanium could differ substantially from the one listed in Table 2. Notice that, even though the SGSL does not possess a global cubic symmetry, each of the individual layers (Si and Ge) does, so the radiation process takes place following Eq. (7) within each of the layers, and the resulting optical intensity is the piecewise addition of the contributions from each layer. This approach gives a rough estimate of the intensity of the field, and does not affect the frequency nor the Brillouin-active nature of a given acoustic mode (see, for example, Refs. [21,42,43]). A detailed electromagnetic model of the photoelastic process in a SL is outside the scope of the present paper, but a very thorough analysis can be found in [43] for a general case in terms of the wavelengths and phonon wave-vectors involved.

2.3. Discussion

According to Eq. (7), in-plane Brillouin scattering along the X-axis can only occur for FAPMs that have a displacement component along that axis, $\Psi_x^{\pm N}$, and the scattering is determined by the component, π_{12}, solely. Therefore, the transverse acoustic modes, polarized along the Z- and Y-axes ($\Psi_{y,z}^{\pm N}$), are not Brillouin-active. The scattering is isotropic along the Y- and Z-directions, i.e. incident and scattered light have the same polarization, along these axes. The longitudinal–transverse modes are responsible for Brillouin scattering only through their longitudinal component, $\Psi_x^{\pm N}$. The amplitude of the radiation produced by a FAPM, $\Psi_x^{\pm N}$, which induces a polarization given by (7), is proportional to the following integral [42]:

$$I_{y,z} \propto \frac{k_B T}{\rho v^2}\cdot\int_0^d |\vec{p}_{y,z}|^2 \mathrm{d}z \tag{8}$$

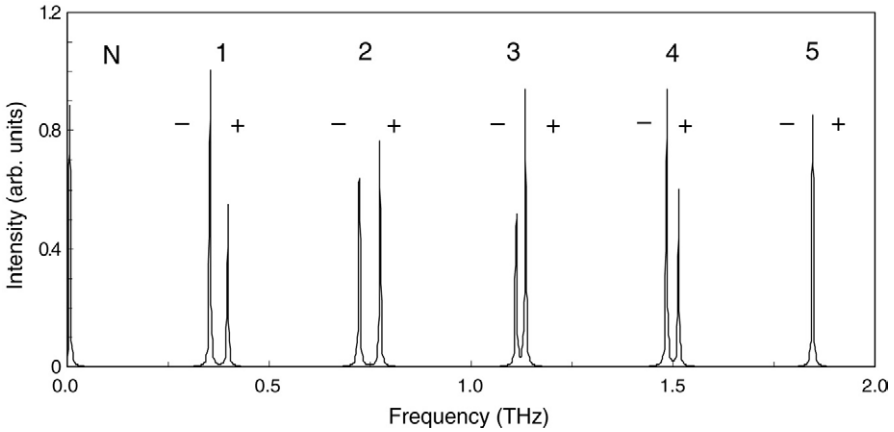

Fig. 6. Brillouin spectrum from close to zone-center TA-FAPMs in a Si_xGe_x superlattice. The modes are from Fig. 2 above. All modes are active and present doublet structure. The label N designates the doublets, as detailed in the text. The doublet $N = 5$ is not resolvable, although it is not degenerate.

where k_B is Boltzmann's constant, T is temperature (Kelvin), ρ is the average density of the material, and v is the group velocity of the wave, $\Psi_x^{\pm N}$. Expression (8) is valid for long wavelength acoustic waves (i.e. $\vec{k}$ close to zone-center), so that the changes in polarizability induced by the acoustic displacement occur through many layers of the SL. This is the case for Brillouin/Raman scattering. Furthermore, the microscopic structure of the SLs of interest here is of only a few hundredths of nm, much smaller than the wavelength of the optical fields considered (1.5–2 μm); therefore, the SL can be treated like an homogeneous medium with effective photoelastic and dielectric constants (Eq. (7)). The latter have been factored out of the right hand side in expression (8) using the proportionality symbol. The integral in expression (8) therefore is proportional to an average value of the square of the Stokes polarization amplitude, induced by the interaction between the incident pump, and the acoustic wave. A thorough elaboration of the electromagnetic theory of an infinite SL is given in [43], where the case for short wavelength acoustic modes is presented, and boundary conditions are applied to each layer of the SL. The constant factor in front of the integral in expression (8) relates to the absolute amplitude of the FAPM, $\Psi_x^{\pm N}$ (the functions shown in Fig. 2 are normalized). This factor is solely related to the material dynamics and not the incident nor scattered electric fields. The acoustic wave amplitude accounts for the internal energy of the material, which is proportional to the factor k_BT, and inversely proportional to the wave's kinetic energy, in order to satisfy the first law of thermodynamics as it applies to the energy transport of the acoustic wave. The significance of this factor will be discussed further below, when the analysis of the frequency bandgaps is introduced. Finally, let us mention that the presence of stress (discussed further below in this section) will modify slightly expression (8) through both the photoelastic constant, regulating the polarization term inside the integral, and the acoustic mode velocities, in the coefficient. Since these effects are of secondary nature even in the case of SiGe SLs, and they are not related to a breakup of symmetry (as discussed below), they will not be considered any further.

The optical spectrum of the $\Psi_x^{\pm N}$ FAPMs, resulting by applying expression (8) to the modes shown in Fig. 2, is depicted in Fig. 6. The case considered in the figure is forward scattering along the x-direction, with an incident/Stokes polarization along the TM mode of the SGP slab (z-axis). This configuration will be denoted, in short, by $X(ZZ)X$. The amplitude of the phonon

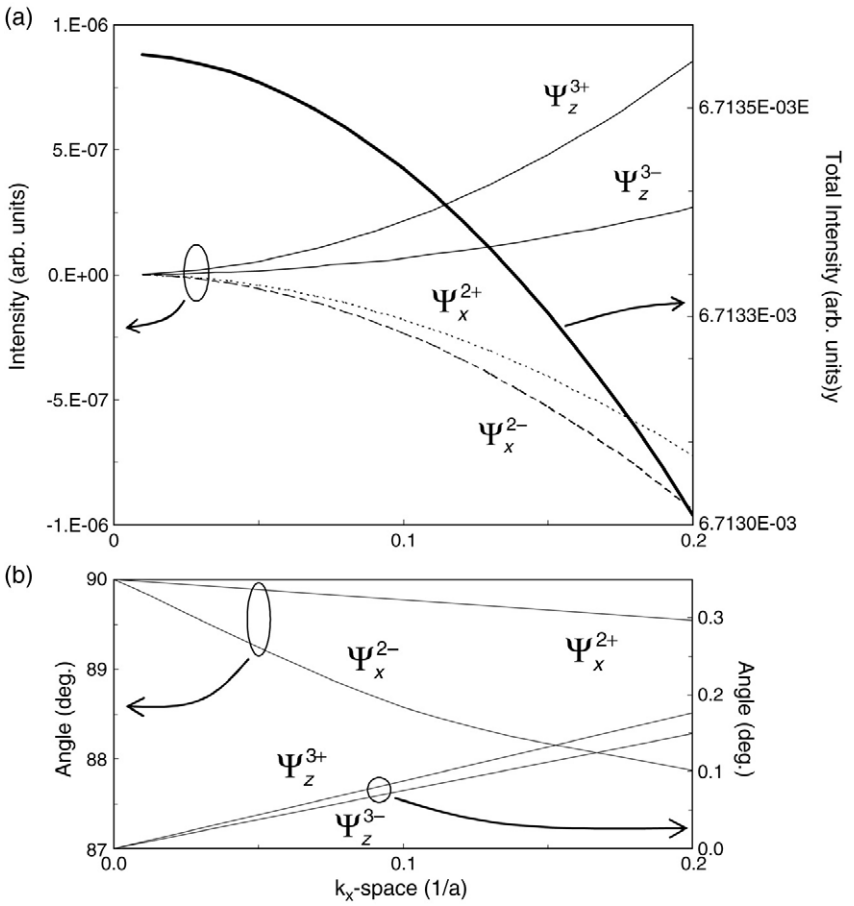

Fig. 7. (a) Brillouin/Raman intensities of the four solutions, $\psi_x^{2\pm}$, $\psi_z^{3\pm}$ at ∼0.8 THz (Figs. 4 and 5). The two components ($\psi_z^{\pm 3}$) become optically active with a finite value of k_x, as a longitudinal component appears in the vibration mode. The curves for the two functions $\psi_x^{2\pm}$ are referenced to zero, for illustration purposes. The Brillouin /Raman amplitude, at $k_x = 0$, is 4.4×10^{-3}, for ψ_x^{-2}, and 2.2×10^{-3}, for ψ_x^{+2}. (b) The angle of each displacement function, $\Psi_{x,z}^{\pm N}$, relative to the z-axis, as a function of k_x. For $k_x \neq 0$, the subscript x, z becomes nominal, and all four wave-functions have components along both x- and z-axes.

wave-vector has been factored out of the intensity, so only relative intensities are considered. A lorentzian linewidth of 6 GHz has been assumed for all the modes. The Brillouin/Raman peaks appear as doublets, reproducing, at $k_x \sim 0$, the zone-center gap of the transverse acoustic modes (cf. Fig. 3). Notice the spectral resolution required to distinguish between the two components of a doublet line (<100 GHz). Fig. 7(a) shows the integral of the Brillouin/Raman induced-polarizability, for the same wave-functions $\Psi_{x,z}^{\pm N}$ depicted in Fig. 5, as a function of the "mixing" wave-vector, k_x. The interesting feature is that, for $k_x \neq 0$, all four waves are Brillouin/Raman active. The reason for this is that all four wave-functions, $\Psi_{x,z}^{\pm N}$, have a component along the x-axis for a finite value of k_x. Therefore, the subscript x, z in the label for the wave-functions, $\Psi_{x,z}^{\pm N}$, is purely nominal, for $k_x \neq 0$. The sum of the optical intensities of the four wave-functions, $\Psi_{x,z}^{\pm N}$, decreases marginally as k_x grows (by about 0.01%). Note that the region of interest is

$0 < k_x < 0.1 \cdot (1/a)$, which is the region allowed by momentum conservation in Brillouin/Raman processes. The effect is therefore more pronounced in back-scattering configurations. Fig. 7(b) illustrates the effect of "mixing", as the value of k_x increases. At zone-center, $\Psi_{x,z}^{\pm N}$ have orthogonally polarized displacements, along the x- and z-axes, respectively. As k_x increases, the angle between the solutions $\Psi_z^{\pm N}$ and $\Psi_x^{\pm N}$ decreases, and each of the wave-functions (x, z) develops a component in the orthogonal axis $(z, x$, respectively).

The spectrum shown in Fig. 6 presents the interesting possibility of creating a multiple-channel Brillouin amplifier, based on a SGSL, whereby the channel spacing, or FSR, is determined by the frequency spacing of the Brillouin-active "doublets" in the spectrum. These channels are almost evenly spaced for the first few modes; their spacing being a function of the periodicity of the SGSL, as will be demonstrated below. Notice also that the spectral range of the first active mode can be conveniently shifted close to the pump frequency. This would remove optical dispersion issues in the implementation of the Raman/Brillouin phenomenon for SGP-based waveguides. Therefore, the application of parametric frequency conversion in such waveguides is possible, via four-wave-mixing (CARS [2,3]), where phase matching between Stokes, anti-Stokes and pump fields is crucial. To further explore the potential for spectrally modifying the Brillouin/Raman characteristics of the SGSL, Fig. 8 shows the shift of the frequencies for Brillouin active modes, in the X(ZZ)X scattering configuration, as a function of the relative silicon content of the SGSL, calculated close to zone-center ($k_x = 0.01 \cdot (1/a)$). It can be seen that the frequency spacing between the active modes is almost doubled by increasing the thickness of the Si layer, relative to the Ge layer. Note that the overall thickness of the SL period remains unchanged. As expected, the structure of the active modes remains the same for different values of d_a, since changing the thickness of the silicon layer, relative to germanium, does not affect the symmetry of the SGSL. The frequency range of the first active mode is also displaced further apart from the pump laser frequency, as d_a grows. The important result here is that the variation of the spectral features is clearly smooth, relative to fairly substantial changes in the SGSL composition.

Figs. 6 and 8 show that acoustic vibrations in the tera-Hertz domain can generate optical radiation in a SGSL waveguide, once a suitable choice of lattice periodicity and relative Si/Ge concentration is made. In the case of stimulated Brillouin/Raman scattering, the optical radiation would be the driving force of the acoustic vibrations in the material. Fig. 8 also reflects the well known fact that, at zone-center, the frequency bandgap formed by the acoustic modes of a superlattice is a function of the lattice periodicity, d_a/d [23,24]. An oscillatory behavior is seen, with a pattern that has a number of nodes equal to the number, N, assigned to each doublet in the manner discussed above. For certain values of the periodicity, the bandgap reduces to a negligible value (zero, in the case $k_z = k_x = 0$). Note that, since these are zone-center effects, they will be more pronounced for forward scattering, although they are not ruled out for backward scattering processes. To have a quantitative insight of the region in phonon phase space that Brillouin/Raman effects take place, let us consider the following example. Assuming an incident photon at $\lambda_i = 1.55$ μm, producing a Brillouin scattered acoustic phonon with a frequency of ∼1 THz (Fig. 6), this phonon has a momentum determined by conservation laws corresponding to ∼5% of the Brillouin zone, in backscattering configuration, and less than 0.01% of the BZ, in a forward scattering configuration. This justifies the assumption throughout the paper that only zone-center phonons have relevance for the analysis presented. Fig. 9 shows this bandgap "pinching" effect more clearly, for $N = 1, 2, 3$. It is seen that this "pinching" effect, observed and predicted for longitudinal modes along the z-axis, has a very similar behavior for in-plane, longitudinal acoustic modes (along the x-axis of the superlattice). The curves labeled "b" in

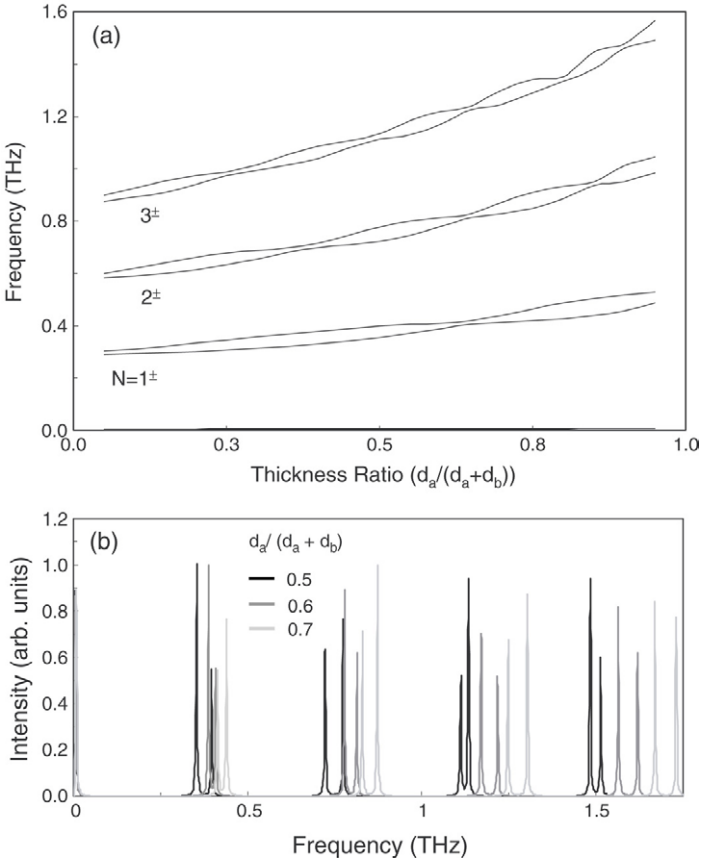

Fig. 8. (a) Variation of the Brillouin-active mode frequencies with respect to the relative thickness of the silicon–germanium layers. (b) Frequency spectrum of Brillouin/Raman peaks from the SGSL at zone-center, for different silicon layer thicknesses. The spectral shift is shown for the specific case of the doublets, $N = 1, 2, 3, 4$, given three values of $d_a/(d_a + d_b) = 0.5, 0.6, 0.7$. The frequency shift is not homogeneous, but the spectral features are preserved.

Fig. 9, correspond to a calculation of the frequency bandgap, Ω_N, following a formula suggested by Jusserand et al., valid in the limit $k_z = k_x = 0$ [23],

$$\Omega_N = \varepsilon \frac{v}{d} \sin\left(\frac{N\pi(1-d_a)\cdot v_{\mathrm{Si}}}{(1-d_a)v_{\mathrm{Si}} + d_a v_{\mathrm{Ge}}}\right) \tag{9}$$

where $d/v = (d_a/v_{\mathrm{Si}}) + (d_b/v_{\mathrm{Ge}})$, and ε is the only fitting parameter used (=0.06). We now move on to discuss the intensity of the Brillouin/Raman active modes, as a function of the layer thickness, d_a. In expression (8) above, the factor, $k_B T/\rho v^2$, was introduced to account for the amplitude of the FAPM. Going a step further, the group velocity of the FAPM, v, is directly proportional to the frequency bandgap, Ω_N [24]; the result is a dependence of the radiation intensity on d_a, which needs to be accounted for. Fig. 10 shows the calculation of scattering intensity for the first three doublets in Fig. 8, as a function of d_a, using expression (8) and Eq. (9). Each curve was obtained by adding the contribution of the two members of a single doublet. A quite significant intensity enhancement is predicted, for all N, at $d_a = 0.65$, which is an important specification to keep in mind for design purposes, in any SGSL-based waveguide.

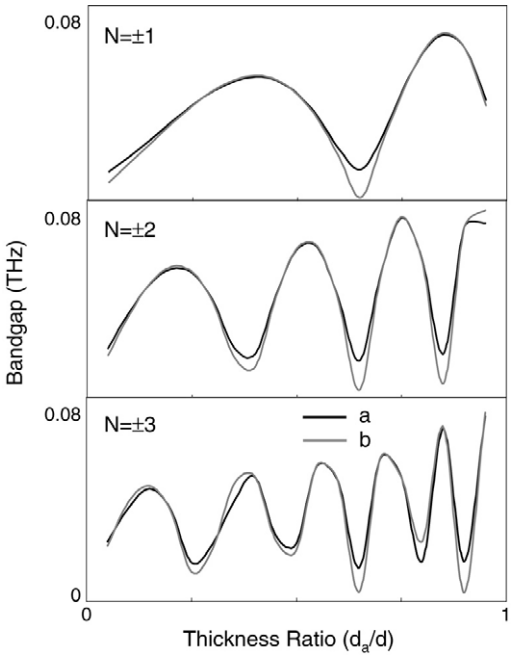

Fig. 9. Bandgap "pinching" for in-plane propagating acoustic waves, as a function of SL periodicity. (a) Results obtained directly from the levels depicted in Fig. 8(a) ($k_z = 0.1, k_x = 0.01$). (b) Approximation using Eq. (9). The assumption is $k_z = k_x = 0$.

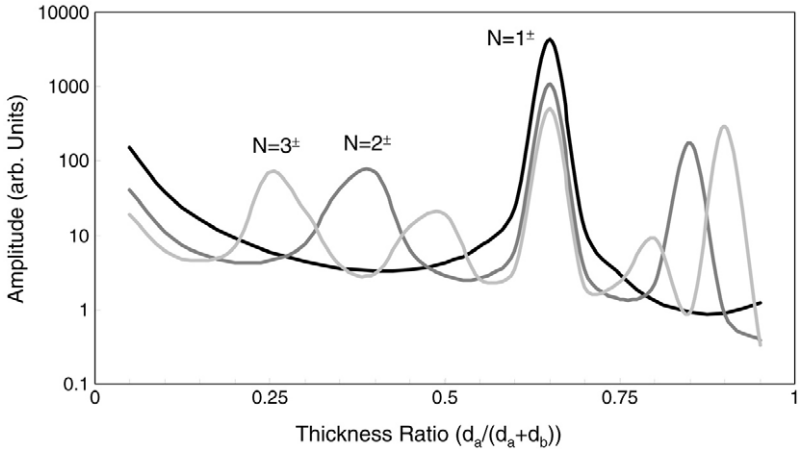

Fig. 10. Relative intensity of Brillouin scattering, from a SGSL with varying relative thicknesses of Si and Ge. The curves are obtained using expression (8), and Eq. (9) for the bandgap calculation. Notice the resonance, for all N, at $d_a/(d_a + d_b) = 0.65$.

The results presented so far have not accounted for the presence of stress, which is a well-known fact in SGPs. It is expected that the spectral changes induced in the Brillouin/Raman response of the material, due to stress, consist mainly in a frequency shift and varying amounts of broadening [44]. In essence, stress induces anharmonicity in the inter-atomic potential, which

is treated through the Gruneisen parameters of each material. By *definition*, these parameters describe the rate of shift in frequency of both acoustic and optical phonons in the material, with respect to strain. In the case of Si and Ge, the largest shift expected occurs for longitudinal acoustic phonons [45,46] and is less than 2%, about an order of magnitude smaller than the doublet splitting, shown in Fig. 6. These effects will have to be accounted for when a specific device is designed and rigorous performance specifications must be met. However, the possibility of using multiple spectral lines arbitrarily separated from one another, for implementing nonlinear Brillouin/Raman scattering, as demonstrated heretofore, is still valid.

Another relevant issue that stress brings into consideration is the feasibility of fabricating such devices. This is especially important in the light of the additional requirement for the SGSL structure to sustain a fundamental optical mode in the near-infrared domain ($\lambda = 1.5\,\mu\text{m}$). Many references have demonstrated the feasibility of fabricating SGSL structures with thicknesses of up to 200–500 nm, which are structurally stable [47]. These dimensions are well within the lower limit of state-of-the-art waveguide fabrication capabilities, and in the limit of optical mode confinement for the refractive index of Si and Ge. The challenge, however, is not a minor one.

Stress produces strain, as determined by the compliance tensor, $\bar{S}$, which is defined by [25]

$$\bar{e} = \bar{S} \otimes \bar{\chi}. \tag{10}$$

This is a static contribution to strain, and therefore it has no direct effect in the optical scattering efficiency. However, nonlinear contributions to the elasto-optic tensor, π, in the presence of strain, could be estimated by atomic-model calculations. This would combine conveniently with the observed high carrier mobility induced by stress in SGP-based MOSFETS [48,49].

3. Summary

In summary, we have shown that optical scattering from Raman-active acoustic phonon modes in SGSL offers an opportunity to modify the spectrum of Raman based silicon waveguide devices. The treatment of the Raman/Brillouin phenomenon for the in-plane forward scattering geometry, the most common geometry for waveguide devices, has been presented here. In addition to calculating the spectrum and the efficiency of Raman-active modes in these structures, it was found that the "bandgap pinching" effect leads to specific layer thicknesses for Si and Ge that optimize the efficiency of the optical process. The results are based on the continuum model for the FAPMs of the SGSL, and a piecewise implementation of the photoelastic model for cubic crystals. Absolute scattering intensities have not been calculated, but a clear resonance condition is identified for $d_a/d = 0.65$. More importantly, it has been demonstrated that the Brillouin spectrum constitutes a comb-frequency profile that can be adjusted in frequency spacing (or "free spectral range"), and in separation from the pump frequency. The adjustment is achieved by tailoring the relative thicknesses of the Si and Ge layers in the SGSL. Stress has been recognized for its potential enhancement of the scattering amplitudes, but further confirmation should be provided by atomic model refinement of the photoelastic model.

Acknowledgement

The authors wish to acknowledge the support of Dr. Jagdeep Shah of DARPA for the realization of this project.

References

[1] R. Claps, D. Dimitropoulos, V. Raghunathan, Y. Han, B. Jalali, Opt. Express 11 (2003) 1731–1739. http://www.opticsexpress.org/abstract.cfm?URI=OPEX-11-15-1731.
[2] R. Claps, V. Raghunathan, D. Dimitropoulos, B. Jalali, Opt. Express 11 (2003) 2862–2872. http://www.opticsexpress.org/abstract.cfm?URI=OPEX-11-22-2862.
[3] V. Raghunathan, R. Claps, D. Dimitropoulos, B. Jalali, Appl. Phys. Lett. 85 (34) (2004).
[4] O. Boyraz, B. Jalali, Opt. Express 12 (2004) 5269–5273. http://www.opticsexpress.org/abstract.cfm?URI=OPEX-12-21-5269.
[5] Q. Xu, V.R. Almeida, M. Lipson, Opt. Express 12 (2004) 4437–4442. http://www.opticsexpress.org/abstract.cfm?URI=OPEX-12-19-4437.
[6] K.K. Lee, D.R. Lim, L.C. Kimerling, J. Shin, F. Cerrina, Opt. Lett. 26 (23) (2001) 1888–1890.
[7] R.L. Espinola, J.I. Dadap, R.M. Osgood Jr., S.J. McNab, Y.A. Vlasov, Opt. Express 12 (2004) 3713–3718. http://www.opticsexpress.org/abstract.cfm?URI=OPEX-12-16-3713.
[8] V.R. Almeida, R.R. Panepucci, M. Lipson, Opt. Lett. 28 (15) (2003) 1302–1304.
[9] S.M. Spillane, T.J. Kippenberg, K.J. Vahala, Nature 415 (2002) 621–623.
[10] A.B. Matsko, A.A. Savchenkov, R.J. Letargat, V.S. Ilchenko, L. Maleki, J. Opt. B: Quantum Semiclass. Opt. 5 (2003) 272–278.
[11] A. Fainstein, B. Jusserand, V. Thierry-Mieg, Phys. Rev. Lett. 75 (1995) 3764.
[12] D. Harame (Ed.), SiGe Proceedings of the ECS conference, Honolulu, Hawaii, 2004.
[13] L. Friedman, G. Sun, R. Soref, Appl. Phys. Lett. 78 (4) (2001) 401.
[14] B. Jusserand, M. Cardona, Raman Spectroscopy of vibrations in superlattices, in: M. Cardona, G. Guntherodt (Eds.), Light Scattering in Solids V: Superlattices and Other Microstructures, in: Topics in Applied Physics, vol. 66, Springer Verlag, Berlin, 1989, pp. 49–152 (Chapter 3).
[15] M.A. Araujo, E. Ribeiro, P.A. Schulz, F. Cerdeira, J. Raman Spectrosc. 27 (3–4) (1996) 257–263.
[16] R.A. Ghanbari, J.D. White, G. Fasol, C.J. Gibbings, C.G. Tuppen, Phys. Rev. B 42 (11) (1990) 7033.
[17] R. Schorer, G. Abstreiter, S. de Gironcoli, E. Molinari, H. Kibbel, H. Presting, Phys. Rev. B 49 (8) (1994) 5406–5414.
[18] R.W. Syme, D.J. Lockwood, J.M. Baribeau, Phys. Rev. B. 59 (3) (1999) 2207.
[19] T.P. Pearsall, J. Bevk, L.C. Feldman, J.M. Bonar, J.P. Mannaerts, A. Ourmazd, Phys. Rev. Lett. 58 (1987) 729.
[20] U. Menczigar, G. Abstreiter, J. Olajos, H. Grimmeis, H. Kibbel, H. Presting, Phys. Rev. B 47 (4) (1993) 4099.
[21] R. Schorer, G. Abstreiter, S. de Gironcoli, E. Molinari, H. Kibbel, E. Kasper, Solid State Electron. 37 (4–6) (1994) 757.
[22] R. Schorer, W. Wegscheider, K. Eberl, Thin Solid Films 222 (1992) 269.
[23] B. Jusserand, D. Paquet, F. Mollot, F. Alexandre, G. Le Roux, Phys. Rev. B 35 (6) (1987) 2808–2817.
[24] C. Colvard, T.A. Gant, M.V. Klein, R. Merlin, R. Fischer, H. Morkoc, A.C. Gossard, Phys. Rev. B 31 (4) (1985) 2080–2091.
[25] Y. Yu Peter, M. Cardona, Fundamentals of Semiconductors, 3rd edition, Springer, Berlin, 2001.
[26] B. Zhu, K.A. Chao, Phys. Rev. B 36 (9) (1987) 4906.
[27] S. Go, H. Bilz, M. Cardona, Phys. Rev. Lett. 34 (10) (1975) 580.
[28] S. Tamura, J.P. Wolfe, Phys. Rev. B. 35 (5) (1987) 2528–2531.
[29] S.M. Rytov, Sov. Phys. Acoust. 2 (68) (1956).
[30] B. Djafari-Rouhani, L. Dobrzynski, O. Hardouin Duparc, R.E. Camley, A.A. Maradudin, Phys. Rev. B 28 (4) (1983) 1711–1720.
[31] E.L. Ivchenko, G. Pikus, Superlattices and Other Heterostructures, in: Springer Series in Solid-State Sciences, vol. 110, Springer-Verlag, Berlin, Heidelberg, ISBN: 3-540-58197-9, 1995.
[32] S. Mizuno, S.-I. Tamura, Phys. Rev B 45 (1992) 734–741.
[33] J.I. Dadap, R.L. Espinola, R.M. Osgood Jr., S.J. McNab, Y.A. Vlasov, Opt. Lett. 29 (23) (2004) 2755–2757.
[34] G. Chen, Phys. Rev. B 57 (1998) 14958–14973.
[35] P. Hyldgaard, G.D. Mahan, Phys. Rev. B 56 (1997) 10754.
[36] A. Balandin, K.L. Wang, Phys. Rev. B 58 (1998) 1544–1549.
[37] L.D. Hicks, M.S. Dresselhaus, Phys. Rev. B 47 (1993) 12727–12731.
[38] M. Trigo, A. Bruchhausen, A. Fainstein, B. Jusserand, V. Thierry-Mieg, Phys. Rev. Lett. 89 (22) (2002) 227402-1.
[39] M. Trigo, A. Fainstein, B. Jusserand, V. Thierry-Mieg, Phys. Rev. B 66 (2002) 125311.
[40] S.M. Komirenko, K.W. Kim, M.A. Stroscio, M. Dutta, Phys. Rev. B 59 (7) (1999) 5013.
[41] G.B. Benedek, K. Fritsch, Phys. Rev. 149 (2) (1966) 647–662.

[42] Z.V. Popovic, J. Spitzer, T. Ruf, M. Cardona, R. Notzel, K. Ploog, Phys. Rev. B 48 (3) (1993) 1659–1664.
[43] J. He, B. Djafari-Rouhani, J. Sapriel, Phys. Rev. B 37 (8) (1988) 4086–4098.
[44] O. Lazarenkova, P. von Allmen, F. Oyafuso, S. Lee, G. Klimeck, Superlatt. Microstruct. 34 (3–6) (2003) 553.
[45] K. Kutsukake, N. Usami, T. Ujihara, K. Fujiwara, G. Sazaki, K. Nakajima, Appl. Phys. Lett. 85 (8) (2004) 1335–1337.
[46] T. Soma, H. Matuso, Y. Saitoh, Solid State Commun. 39 (1981) 913.
[47] F.K. LeGoues, B.S. Meyeron, F.J. Morar, Phys. Rev. Lett. 66 (1991) 2903.
[48] S.-I. Takagi, J.L. Hoyt, J.J. Welser, J.F. Gibbons, J. Appl. Phys. 80 (3) (1996) 1567–1577.
[49] R. Oberhuber, G. Zandler, P. Vogl, Phys. Rev. B 58 (15) (1998) 9941–9948.